Journal of Space Safety Engineering 13 (2026) 48–58

Contents lists available at ScienceDirect

Journal of Space Safety Engineering

journal homepage: www.elsevier.com/locate/jsse

Multiphysics modelling of academic potassium nitrate–sucrose solid rocket motors for thermomechanical analysis ☆,†,‡,§,¶

Sebastian Valencia [a,b,d,*], Jaime Enrique Orduy [b,c], Santiago Garcia de la Peña [a]

[a] Cranfield University, Cranfield, Bedfordshire, MK43, United Kingdom
[b] Fundacion Universitaria Los Libertadores, Bogotá, D.C, 110110, Colombia
[c] National Institute of Space Research (INPE), São José dos Campos, SP, 12227-010, Brazil
[d] Escuela de Aviación del Ejército (ESAVE), Bogotá, D.C, 110110, Colombia

ARTICLE INFO

Article history:
Received 2 July 2025
Received in revised form 4 November 2025
Accepted 18 December 2025
Available online 22 January 2026

Keywords:
SRM
KNSU
Casing properties
Multi-physics

ABSTRACT

This work presents an integrated Multiphysics framework for the design and thermo-structural evaluation of an academic potassium nitrate–sucrose (KNSU) solid rocket motor (SRM). The study bridges a major gap between industrial-grade SRM modelling and educational-scale applications by combining internal ballistics, heat-transfer analysis, and finite element structural simulation within a unified computational environment. The propellant burn rate is modelled through Saint-Robert's law, while transient chamber pressure and nozzle erosion are coupled with the structural solver to evaluate stresses, deformation, and safety margins under operational conditions. Thermal and mechanical load interactions are assessed using temperature-dependent material properties for AISI 1020 steel, and the viscoelastic response of the propellant is represented through a Prony-series formulation. Results indicate a peak chamber pressure of approximately 8.6 MPa during ignition, followed by a steady-state regime near 4.8 MPa, with corresponding maximum casing stresses below 0.5 σ_y, ensuring safe operation. Comparative analysis against NASA SP-125 empirical correlations shows less than 5% deviation in predicted thrust and impulse, validating the model accuracy. The framework offers an accessible yet rigorous methodology for academic and laboratory-scale SRM design, supporting both educational experimentation and early-stage research in solid propulsion. Future work will incorporate experimental validation, uncertainty quantification, and ablation–viscoelastic coupling to further improve predictive fidelity.

© 2026 International Association for the Advancement of Space Safety. Published by Elsevier Ltd. This is an open access article under the CC BY license (http://creativecommons.org/licenses/by/4.0/)

1. Introduction

Solid rocket motors (SRMs) remain fundamental to aerospace propulsion—used in applications from booster stages to reaction control—because they deliver high thrust impulsively with simple, reliable hardware and no complex fueling infrastructure [1,2]. Yet, despite extensive industrial development, research on small-scale and educational SRMs is comparatively sparse, leaving room to strengthen hands-on training and low-risk experimental development in academic settings.

SRMs operate by converting the chemical energy of a compacted solid propellant into hot, high-pressure gases that are accelerated through a nozzle to produce thrust [3]. Although the literature contains many investigations of full-scale, industrial SRM designs and their performance, comparatively few works target prototype motors optimized for safety, low cost, and reproducibility in teaching laboratories [4,5].

This paper fills that gap by presenting a computationally validated design for a compact SRM using potassium-nitrate/sucrose (KNSU) propellant with AISI 1020/AISI 4140 steel structural components (see Fig. 1). KNSU offers a practical balance of energy and manageable combustion characteristics for academic use [6–9]. The study couples multiphysics tools—thermochemical modelling, Saint-Robert's burn-rate formulation [10,11], and transient finite-

☆ Graduate MSc Astronautics and Space Engineering, School of Aerospace, Transport and Manufacturing, Cranfield University, Cranfield, MK48, Bedfordshire, United Kingdom.

† Associate I lecturer, Engineering and Basic Sciences, Fundacion Universitaria Los Libertadores, Bogotá, D.C, Colombia.

† Assistant I lecturer, Aeronautical Engineering, Escuela de Aviación del Ejército, CEMIL, Bogotá, D.C, Colombia.

¶ Assistant II lecturer, Engineering and Basic Sciences, Fundacion Universitaria Los Libertadores, Bogotá, D.C, Colombia.

¶ PhD Graduate, National Institute of Space Research (INPE), Brazil.

* Corresponding author at: Fundacion Universitaria Los Libertadores, Bogotá, D.C, 110110, Colombia.

E-mail addresses: s.valencia.109@cranfield.ac.uk (S. Valencia), jeorduyr@libertadores.edu.co (J.E. Orduy), s.garciadelapena.568@cranfield.ac.uk (S. Garcia de la Peña).

https://doi.org/10.1016/j.jsse.2025.12.003
2468-8967/© 2026 International Association for the Advancement of Space Safety. Published by Elsevier Ltd. This is an open access article under the CC BY license (http://creativecommons.org/licenses/by/4.0/)

Nomenclature

DMA	Dynamic Mechanical Analysis.
KNSU	Potassium Nitrate – Sucrose
SRM	Solid Rocket Motor.

element structural analysis—to predict chamber pressure histories, coupled thermal–mechanical loads, and the resulting structural response during operation [12].

A distinguishing feature of this research lies in its comprehensive modelling of viscoelastic deformation [13] within the SRM grain structure, employing a Prony series formulation to capture time-dependent strain evolution under coupled thermal and mechanical loading [14,15]. This approach, typically reserved for advanced propellant characterizations [16,17], underscores the academic ambition to simulate real-world rocket behaviour with high fidelity. The design methodology incorporates optimization algorithms (e.g., Monte Carlo methods) and mesh convergence validation, ensuring robustness in geometric and structural assessment [7,18]. Moreover, by benchmarking the simulated SRM performance against both academic references [2,19] and industrial standards [15], this study not only identifies design limitations (e.g., safety margins and thrust shortfalls) but also proposes future enhancement pathways such as grain geometry refinement, thermal barrier coatings, and high-temperature material substitution.

1.1. Reverse design and multiphysics modelling advances in educational SRMs

Recent advances in SRM design have moved toward Multiphysics and machine learning-driven frameworks capable of capturing the nonlinear coupling between geometry, internal ballistics, and thermomechanical response. Li et al. on [20] proposed a reverse design methodology for propellant grains using an *evolutionary neural network*, enabling automatic optimisation of unconventional geometries without relying on predefined templates such as star or slotted-tube configurations [20]. Their approach integrates the *Poisson–Eikonal–Finite Element (PEF)* method with a *phase-field neural representation*, allowing the automatic generation and burn-back analysis of irregular grain shapes through fixed unstructured meshes. This neural encoding of grain geometry offers an adaptable basis for the inclusion of thermoelastic and viscoelastic effects in academic hybrid propellants like KNSU *(KNO_3–$C_{12}H_{22}O_{11}$)*.

Complementary studies have demonstrated that machine learning-assisted SRM modelling can significantly enhance predictive accuracy and reduce computational overhead in nonlinear burn-back and stress analysis. For instance, studies by Abelardo on [20] developed a hybrid optimization architecture coupling genetic algorithms with surrogate thermofluidic models for improved internal ballistic predictions in small rocket motors, Similarly, Wang et al, [21] introduced a Multiphysics-coupled FEM framework that captures the interaction between thermal gradients, structural deformation, and viscoelastic relaxation in SRMs, offering better alignment with experimental deformation fields. More recently, Tang et al. (2025) on [22] proposed a computationally efficient Multiphysics solver for coupled *thermal–chemical–structural* transients in miniature solid motors, demonstrating substantial error reduction in propellant stress and strain estimations.

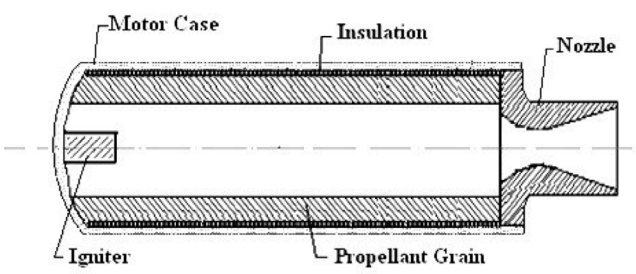

Fig. 1. Schematic of an SRM [15].

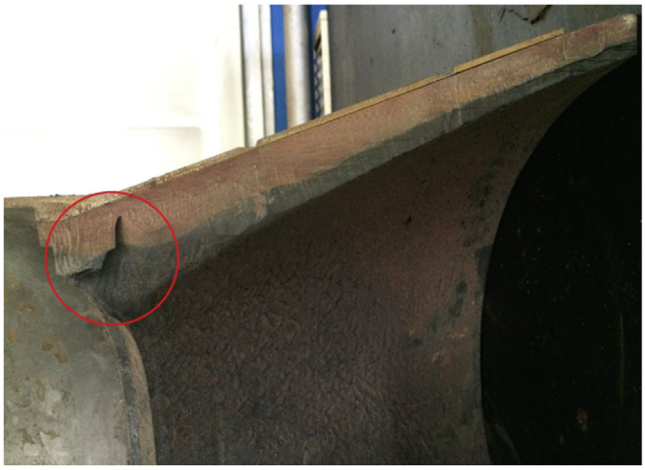

Fig. 2. Divergent region after the experiment [23].

These developments converge on the need for unified educational frameworks where *academic SRMs*—such as KNSU-based systems—can be modelled through accessible Multiphysics simulations combining heat transfer**,** combustion regression, and structural response. Yet, the complexity of coupling burn-back dynamics with temperature-dependent viscoelastic properties remains underexplored in open-source or educational contexts. Most models assume isotropic or purely elastic behaviour, omitting the time-dependent softening and residual strain accumulation characteristic of sugar-based propellants under thermal cycling.

1.2. Technical gaps in current thermo-structural modelling of academic solid rocket motors

Recent studies (for example, the investigation published in *Energies* on the combustion and flow behaviour of solid propellants) found on [23] demonstrate that even well-developed simulation tools often oversimplify the interactions between internal ballistics, heat transfer, and structural response. Their results show that transient thermal gradients, wall heat flux dynamics and local flow perturbations can lead to non-uniform stress distributions and early onset of material fatigue — phenomena that are rarely captured in standard educational models. The study furthermore highlights that most frameworks assume quasi-steady combustion, neglecting coupling between temperature rise, propellant regression and evolving structural deformation, thereby limiting their validity for realistic motor designs as seen in Fig. 2 [23].

Fig. 2 illustrates the post-firing condition of the divergent section of the solid rocket motor nozzle, highlighting the thermal-mechanical degradation that occurred during combustion. Compared with the convergent region, the divergent portion exhibits less ablation and carbonization, confirming the lower thermal load predicted by the numerical model. However, a localized perforation (circled in red) penetrates the second structural layer, evidencing a flame leak along the insert–insulation interface. This damage validates the authors' conclusion that the 0.2 mm design gap between the insert and the composite insulation was insufficient to prevent gas infiltration, enabling high-temperature flow to propagate through the bonding interface. Consequently, both the pri-

mary leakage path and an alternative path require redesign and tighter manufacturing tolerances. The experimental observation in Fig. 2 therefore corroborates the numerical prediction that interface sealing and coupled thermo-structural behaviour are critical to the long-term integrity of SRM nozzles [23].

Also, recent findings by Huang *et al.* (2023) on [24] revealed that nozzle ablation in solid rocket motors induces complex, time-dependent interactions between internal flow, wall temperature, and thrust, which are not captured in most academic models. Their simulations showed that as ablation progresses, changes in nozzle geometry alter the shock pattern and Mach distribution, leading to local increases in pressure and temperature and a measurable decrease in thrust. However, current educational frameworks typically treat ablation as a steady geometric correction, neglecting this dynamic coupling.

The study also demonstrated that ablation steps generate disturbed flow regions and secondary compression waves, creating non-uniform heat fluxes and stress concentrations that simplified models fail to predict. Additionally, Huang *et al.* highlighted the feedback between ablation and gas thermophysical properties—such as viscosity and thermal conductivity—further influencing wall heat transfer. These findings expose clear gaps in conventional SRM modelling, including (1) the absence of fully coupled transient analysis, (2) omission of local thermo-mechanical effects, and (3) lack of adaptive meshing or moving-boundary approaches.

Addressing these issues requires a new educational Multiphysics framework that integrates real-time ablation–flow coupling and transient thermo-structural feedback to improve both predictive accuracy and training value [24].

1.3. Overview and key contributions

The present study introduces a unified Multiphysics simulation framework for the thermo-mechanical and viscoelastic analysis of academic-scale potassium nitrate–sucrose (KNSU) solid rocket motors (SRMs). The work bridges the gap between professional-grade computational tools and accessible educational models, providing a reproducible methodology for analysing pressure evolution, structural integrity, and material response in small SRMs. Unlike previous studies that treat combustion, thermal conduction, and structural deformation as independent processes, the proposed framework integrates these phenomena within a single transient numerical environment.

Specifically, the model couples the internal ballistics of grain regression, transient heat transfer across the motor chamber, and finite-element structural analysis that incorporates viscoelastic material behaviour calibrated through a simplified Prony-series representation. This approach enables the assessment of stress evolution, deformation, and safety factors under realistic operating conditions while maintaining computational efficiency suitable for academic settings.

2. Computational framework and design methodology of the KNSU solid rocket motor

2.1. Theoretical framework for SRM performance

The theoretical foundation of the present work integrates internal ballistics, thermal transport, and structural response within a single transient numerical framework. In contrast to conventional quasi-steady or one-dimensional educational tools, which assume constant chamber pressure and neglect feedback between combustion and wall deformation, this approach resolves the time-dependent coupling among mass generation, compressible flow, and temperature-induced stress evolution inside the motor casing.

2.1.1. Internal ballistics and propellant regression

Combustion in a solid rocket motor is governed by the regression rate of the propellant surface, r, which depends on the instantaneous chamber pressure $P_c(t)$ according to the empirical Saint Robert's law [25,26]:

$$r = P_C^n \tag{1}$$

where a is the burn-rate coefficient and n is the pressure exponent, typically in the range 0.25 – 0.45 for KNSU propellants.

The total mass flow rate entering the chamber is [26]:

$$m_b = \rho_p A_b r \tag{2}$$

with ρ_p the propellant density and $A_b(t)$ the instantaneous burning area obtained from grain geometry regression. The pressure-time behaviour then follows from mass continuity and nozzle discharge conditions [25]:

$$\frac{dP_c}{dt} = \frac{\gamma R T_c}{V_c}\left(m_b - m_e\right) \tag{3}$$

where m_e is the mass flow rate through the nozzle, γ is the ratio of specific heats, R is the gas constant, T_c the chamber temperature, and V_c the time-varying free volume [25,26].

- Combustion Chamber Pressure

The steady-state chamber pressure P_c is derived from the mass balance between propellant gas generation and nozzle expulsion:

$$P_c = \left(\frac{\rho_p \cdot a \cdot A_b \cdot C^*}{A_t}\right)^{\frac{1}{1-n}} \tag{4}$$

where ρ_ρ is propellant density (1,850 kg/m³ for KNSU), a and n are burn rate coefficients from Saint Robert's Law ($r = aP^n$), A_b is burning surface area, A_t is nozzle throat area, and C^* is the characteristic velocity (1,520 m/s for KNSU) [4,5].

- Thrust Equation

Thrust F is calculated as:

$$F = m \cdot v_e + (\ p_e - p_a) \cdot A_e \tag{5}$$

where $m = \rho_p \cdot r \cdot A_b$ is the mass flow rate, v_e is exhaust velocity, P_e is exit pressure, P_a is ambient pressure, and A_e is nozzle exit area. For under expanded flows ($P_e > P_a$), the second term dominates.

2.1.2. Energy and momentum coupling

The energy conservation equation accounts for heat transfer from the hot gases to the propellant and chamber wall [26,27]:

$$\rho_g c_p \frac{\partial T}{\partial t} + \rho_g u \frac{\partial h}{\partial x} = k_g \frac{\partial^2 T}{\partial x^2} - q_2'' \tag{6}$$

where q_w'' is the convective heat flux at the wall–gas interface, evaluated using a modified Bartz correlation. The resulting temperature field defines the thermal load that drives both casing expansion and viscoelastic creep. The assumption of one-dimensional compressible flow remains valid for slender motors with low divergence half-angles ($< 15°$); however, transient simulations capture axial wave effects and pressure oscillations neglected in steady analytical models [27].

2.1.3. Thermo-mechanical feedback

The pressure history $P_c(t)$ couples with the mechanical stress field through the internal pressure boundary condition on the casing and through temperature-dependent material properties $E(T)$ and $\sigma_y(T)$. The deformation of the chamber slightly alters the free volume V_c, providing weak feedback on $P_c(t)$. This thermo-mechanical loop becomes significant in small-scale educational SRMs where wall thicknesses are comparable to grain diameter, resulting in measurable strain-pressure interactions [26,27].

2.1.4. Novelty of the proposed framework

Unlike earlier frameworks that treat combustion, heat transfer, and structural analysis separately [25,26], the present model explicitly couples the transient energy equation, pressure evolution, and viscoelastic response within a unified computational environment. This allows prediction of peak stress, casing deformation, and internal temperature rise with greater fidelity than quasi-steady educational solvers. The framework also incorporates temperature-dependent material degradation and time-resolved boundary conditions, extending its applicability to safety assessment and design optimization of small, potassium-nitrate–sucrose motors used for instructional and research purposes.

2.2. Material selection and structural criteria

Material selection for the casing and nozzle is a primary determinant of structural integrity and service life in small solid rocket motors. The selection must therefore account not only for room-temperature strength and manufacturability, but also for (1) the temperature dependence of elastic modulus and yield strength, (2) creep resistance under transient high temperature, and (3) fatigue and damage accumulation under repeated thermal–mechanical cycles. In this work the casing and nozzle baseline materials are AISI 1020 (casing) and AISI 4140 (nozzle); the following subsections explain the rationale, identify their high-temperature limitations, propose higher-performance alternatives, and present a simple creep/fatigue screening methodology [28,29].

2.2.1. Temperature-dependent mechanical behaviour (AISI 1020, AISI 4140)

Steel mechanical properties degrade with increasing temperature: elastic modulus $E(T)$ decreases, yield strength $\sigma_y(T)$ falls, and ductility typically increases until microstructural softening and oxidation reduce load-bearing capacity. For engineering assessments, it is essential to treat E and σ_y as functions of temperature rather than constants [29].

Practical engineering points for the chosen alloys:

- AISI 1020 (carbon steel, commonly used for casings):

Selected for ductility, low cost and ease of fabrication. At ambient temperature AISI 1020 exhibits nominal Young's modulus on the order of ∼ 200 GPa and yield strength in the low hundreds of MPa (supplier-specific). Above roughly 400–600°C mechanical strength begins to fall appreciably, and oxidation can compromise section properties. For SRM casings that experience short-duration high-temperature exposure, AISI 1020 is acceptable when protected by insulation and when peak metal temperatures are kept below the conservative limit where $\sigma_y(T)$ has not decreased beyond allowable margins.

The casing must withstand peak von Mises stress σMV , defined as:

$$\sigma MV = \sqrt{\frac{(\sigma_1 - \sigma_2)^2 + (\sigma_2 - \sigma_3)^2 + (\sigma_3 - \sigma_1)^2}{2}} \tag{7}$$

where σ_1, σ_2 , σ_1 are principal stresses. AISI 1020 steel (σ_y=350 MPa) was selected for its ductility and cost-effectiveness, with a safety factor $SF = \sigma_y/\sigma_{VM} \geq 2.0$ [30].

- AISI 4140 (alloy steel, nozzle candidate):

AISI 4140 presents improved high-temperature performance relative to mild steels due to its alloying elements (Cr, Mo). It retains higher yield strength and better hardenability, and is commonly used for nozzle/throat hardware where temperatures approach several hundred°C. Nonetheless, at temperatures approaching 600–800°C (short exposures) creep and strength degradation become non-negligible; therefore, AISI 4140 should be used with either thermal barriers or coatings or be replaced with a more oxidation/creep resistant alloy for aggressive duty cycles.

The nozzle throat experiences stagnation temperatures up to 2,800 K. AISI 4140 steel (σ_y = 655 MPa) was chosen for its high-temperature creep resistance, validated via the Larson-Miller parameter:

$$d_t = K \cdot P_C^{0.8} \cdot t^{0.2} \tag{8}$$

where T is temperature (K) and t is time (hours) [31].

Recommended practice: assemble temperature-dependent curves $E(T)$ and $\sigma_y(T)$ for each material from authoritative sources (mill certificates, ASTM/ISO data, material provider datasheets). Use linear or spline interpolation in the solver; do not assume constant properties for transient thermo-mechanical runs [28].

- Nozzle Aerodynamics and Geometry Optimization

The convergent-divergent (C-D) nozzle design follows the de Laval criterion for supersonic flow:

$$\frac{A_e}{A_t} = \frac{1}{M_e}\left(\frac{2}{y+1}\left(1 + \frac{y-1}{2}M_e^2\right)\right)^{\frac{y+1}{2(y-1)}} \tag{9}$$

where γ = 1.2 (KNSU combustion gases), M_e=2.8 is the design exit Mach number, and A_e/A_t = 8.5. Throat erosion was modeled using the empirical relation:

$$d_t = K \cdot P_C^{0.8} \cdot t^{0.2} \tag{10}$$

with k = 2.5 × 10^{-6} m/(MPa$^{0.8}$· s$^{0.2}$) [6].

2.2.2. Candidate high-temperature substitutes and trade-offs

When the thermal environment or safety target requires improved high-temperature performance, consider higher-performance alloys. Two practical options for small SRM nozzles and critical hardware are [28]:

- **Inconel 625 (Ni-based superalloy):** excellent oxidation and creep resistance up to ∼ 800–900°C, high toughness, and good weldability. Advantages: minimal strength loss in short high-temperature pulses and superior corrosion/oxidation protection. Drawbacks: higher density and cost; more difficult machining—trade-off against weight and budget constraints.
- **Maraging steels (e.g., Maraging 300/350):** ultra-high yield strength after ageing heat treatment and good toughness. Maraging alloys offer high static strength with moderate creep resistance at moderate temperatures; however, their oxidation resistance is lower than Ni-based alloys and may require surface protection for high-temperature exposure.

Therefore, it should pick the lowest cost material that satisfies the maximum metal temperature and required safety factor for the design life. If the nozzle throat experiences repeated exposure above ∼700 K (≈427°C) or if ablation exposes metal surfaces to combustion gases, prefer Inconel or coated high-alloy steels.

2.2.3. Simplified creep and fatigue screening — Larson–Miller approach

For preliminary design and material screening, a compact Larson–Miller parameter (LMP) based approach provides a practical means to estimate time-to-rupture at elevated temperature without full creep testing. Use the following steps as a conservative screening procedure:

Larson–Miller parameter (LMP):

$$LMP = T\left(C + log_{10}t_r\right) \tag{11}$$

where:

- T is the absolute temperature (K) at which creep occurs (use maximum metal temperature),

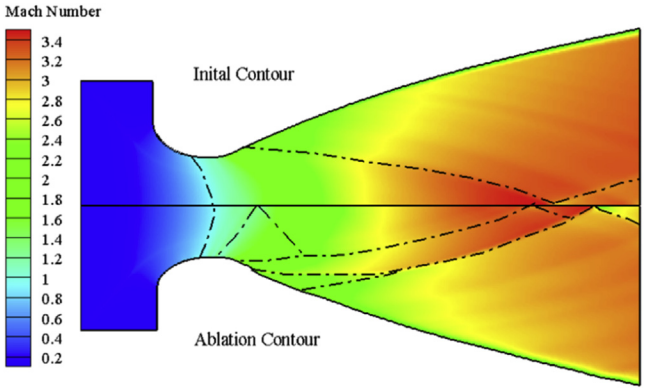

Fig. 3. Mach number distribution of the ground state nozzle before and after ablation [24].

- t_r is time-to-rupture in hours,
- C is a material constant (commonly in the range 20–23 when T is in K and t_r in hours); C must be obtained from experimental creep rupture data for the specific alloy.

2.3. Thermal analysis and heat-transfer coupling

The thermal model couples the convective heating from hot combustion gases, conductive heat transfer through insulation and metal layers, and radiative exchange at exposed surfaces to determine the time-dependent wall temperature field used by the structural solver. Convection at the gas–wall interface is evaluated using a modified Bartz correlation for high-temperature rocket flows, with empirical corrections to account for non-ideal gas properties and near-wall ablation products; radiation is included where exposed hot surfaces and inserts require it. These choices follow the same modelling philosophy used for small KNSU motors and ensure that the dominant heat-transfer modes during ignition and early burn are captured [24].

Fig. 3 from Huang et al. [24] illustrates the impact of nozzle ablation on the internal flow field by comparing Mach number distributions in the original (Initial Contour) and ablated (Ablation Contour) geometries. In the left-hand region of the plot the throat is shown for both the initial and ablated states. The ablation contour exhibits a larger exit diameter and altered expansion profile, which pushes the Mach field lines outward, reduces the peak Mach number at the throat, and redistributes the shock structure downstream. This geometry change leads to a less uniform supersonic flow, locally higher temperature and pressure zones, and reduced effective expansion ratio. From a thermal-analysis standpoint, the shifted Mach contours imply that wall heat–flux distributions also change: regions that originally experienced moderate supersonic acceleration now endure stronger shock impingement and higher stagnation temperatures, increasing convective heat transfer and potentially elevating wall temperature peaks. These changes reinforce the need for transient, geometry-aware heat-transfer modelling, rather than static or steady-state assumptions.

Wall heat flux is computed as a time-series boundary condition for the structural model. For each thermal time step we compute the convective heat flux at the chamber wall, $q''_{conv}(t)$, and the radiative term $q''_{rad}(t)$, and resolve 1-D/2-D conduction through insulation and metal layers to obtain nodal metal temperatures $T(x, t)$. When nozzle ablation or throat erosion is simulated, the moving boundary is handled via a re-meshing or moving-mesh strategy and the local heat flux is adjusted to account for changing wall curvature and local particle loading, following the approach demonstrated for axisymmetric transient ablation in Huang et al. on [24]. This two-way coupling (flow → wall regression → modified flow) is activated in cases where throat recession is expected to change the expansion ratio significantly.

Temperature-dependent material properties (Young's modulus, yield strength, thermal conductivity and specific heat) are mapped onto the structural mesh at each coupling interval. For viscoelastic propellant models the Prony-series parameters are shifted using time–temperature superposition (where experimental DMA data exist) to reflect the effective modulus at the instantaneous temperature field. The transient coupling frequency (how often thermal results are passed to the structural solver and pressure is updated) is selected to resolve the ignition spike — in our computations a coupling interval of 0.01 s with adaptive sub-stepping during the first 0.1 s was used. All thermal runs must include mesh/time-step convergence studies (presented as a short table) and report the Δt used and the maximum nodal temperature for traceability [32].

2.3.1. Heat-transfer mechanisms and modelling assumptions

The thermal field within the academic KNSU solid rocket motor (SRM) was determined by considering the three dominant heat-transfer mechanisms: convection from the combustion gases to the internal wall, conduction through the metallic casing and insulation layers, and radiation from the hot gases and the nozzle throat to the surroundings. Convection was identified as the dominant mode inside the chamber due to high gas velocities and elevated temperatures, whereas conduction governed the temperature gradient through the propellant–insulation–casing interface. Radiative exchange was modelled primarily at the nozzle throat and outer wall, where surface temperatures exceed 1000 K and view factors to the ambient environment become significant [32,33].

To represent the gas–wall interface, a non-slip adiabatic boundary condition was applied to the core flow, and a conjugate heat-transfer approach was adopted to couple the gas-side and wall-side domains. The governing transient heat-conduction equation in cylindrical coordinates was solved using temperature-dependent material properties for both the KNSU propellant and the AISI 1020 steel casing. The internal surface heat flux was defined as the sum of convective and radiative components:

$$q''_{total}(t) = q''_{conv}(t) + q''_{rad}(t) \tag{12}$$

where q''_{conv} arises from turbulent boundary-layer transport and q''_{rad} represents gas and wall radiation exchange. These conditions follow standard small-scale SRM thermal-modelling practices recommended in *Rocket Propulsion Elements* [34] and validated in Cheng et al. [32], who demonstrated that nozzle ablation substantially modifies near-wall thermal loads.

Fig. 4 depicts the full iterative sequence used by the authors to simulate the ablation of a composite nozzle under solid rocket motor conditions. The process begins by assigning initial boundary and material conditions for both the fluid and solid domains: this includes gas inlet pressure/temperature, nozzle wall and structural materials, and an initial geometry. Next, the coupled fluid and solid solvers are executed: the Navier–Stokes equations govern the gas flow, while the solid heat-conduction equation models wall/insulation temperature evolution. From these solutions, the wall temperature, pressure, gas composition and density fields are extracted.

With these fields, the material mass-loss rate is calculated using chemical-kinetics and diffusion-controlled ablation models. The minimal controlling mechanism is selected to determine the effective mass-loss rate, and dividing by local material density yields a linear ablation rate (geometry recession). The heat carried away due to ablation and chemical reaction is then introduced as a source term in the boundary energy equation of the fluid-solid coupling. Mesh updates or dynamic mesh remeshing are employed to adjust the nozzle surface based on the computed recession rate,

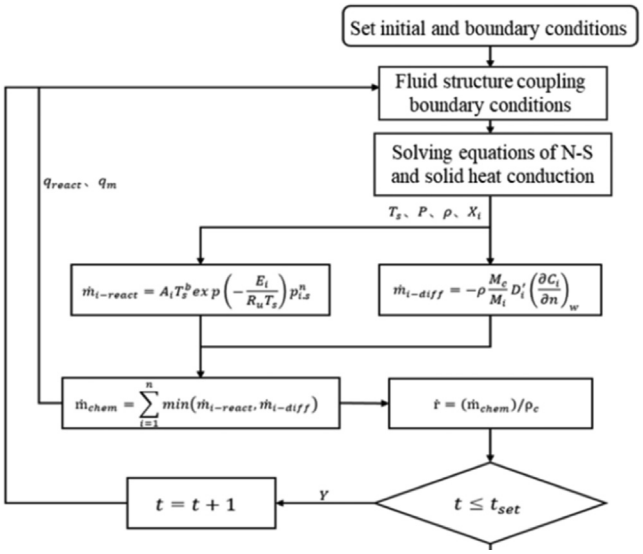

Fig. 4. Unsteady-state ablation calculation process for the composite nozzle.

and the simulation advances in time with semi-implicit time stepping until the target simulation time (18 s) is reached.

The calculation loop thus combines fluid solution → thermal conduction → ablation rate → geometry update → repeat. In essence, this multi-physics coupling ensures that the evolving geometry affects the flow, which in turn affects wall heating and ablation, forming a feedback loop that captures transient changes in nozzle contour, shock structure, and heat flux. By including the ablation-heat feedback and dynamically updated geometry, the model improves fidelity over static approximation methods where nozzle contour is held fixed.

2.4. Finite element analysis (FEA) methodology

The finite element analysis (FEA) of the academic KNSU solid rocket motor (SRM) was performed to evaluate the structural response under coupled pressure and thermal loading throughout the burn cycle. The procedure followed standard aerospace simulation practices: geometry and mesh generation, definition of loads and boundary conditions, transient solution, and numerical validation [28].

2.4.1. Model geometry and meshing

A two-dimensional axisymmetric model was constructed to represent the motor casing, propellant grain, insulation, and nozzle insert. The geometry was simplified to preserve symmetry while retaining critical stress-bearing features such as the case–nozzle junction and aft bulkhead. The domain was discretised using quadratic thermal–structural coupled elements (PLANE223 type in ANSYS). A mesh-refinement study was conducted to determine the optimal element size near the throat and grain interface, where high stress and temperature gradients are expected. The grid convergence index (GCI) was calculated following the method recommended by ASME to ensure mesh independence, with a refinement ratio $r = 1.5$ and acceptable relative error below 2 % [7].

2.4.2. Load definitions and coupling

Transient internal pressure was applied on the chamber wall according to the time-dependent curve obtained from the internal-ballistics solver (2.3). The temperature field from the thermal analysis was mapped as a body-load distribution across the casing thickness, introducing temperature-dependent material properties. To prevent rigid-body motion, the aft-end nodes were fixed axially, and radial displacement was constrained along the symmetry axis. Both mechanical and thermal boundary conditions were synchronised in time, ensuring that the stress evolution reflected realistic ignition transients Huang et al., 2023 [24].

A transient structural-thermal coupled simulation was performed in ANSYS Mechanical™. The governing equation for thermal stress is:

$$\nabla \cdot \left(C : \nabla u\right) + f = \rho \frac{\partial^2 u}{\partial t^2} \tag{13}$$

where **C** is the elasticity tensor, **u** is displacement, f is body force, and $\rho\rho$ is density. Boundary conditions included:

- **Pressure Load:** $P_c = 5.3$ MPa (transient peak)
- **Thermal Load:** Tinner = 2,800 K, Touter = 300 K

Mesh independence was verified using the GCI with Richardson extrapolation [7].

2.4.3. Material models

The casing and nozzle insert were treated as temperature-dependent isotropic materials. For AISI 1020 steel, the elastic modulus, yield strength, and thermal expansion coefficient were updated at each time step from tabulated data. The propellant domain was modelled using a linear viscoelastic constitutive law based on a Prony-series representation derived from Wang et al. [21], enabling simulation of creep and stress relaxation during burn. All material data were implemented as temperature-dependent curves in the engineering data library to maintain continuity between thermal and structural solvers.

2.4.4. Solution strategy

A **transient sequential coupling** scheme was adopted. The nodal temperature field $T(x, t)$ computed in the thermal module served as input for the structural solver, which integrated the governing equilibrium equation:

$$[K(T)]\{u\}(t) = \{F_P(t)\} + \{F_T(T,t)\}, \tag{14}$$

where $[K(T)]$ is the temperature-dependent stiffness matrix, $\{F_P(t)\}$ is the pressure load vector, and $\{F_T(T,t)\}$ represents the thermal-expansion forces. The implicit Newmark-β time-integration method was used for numerical stability, with a baseline time step of $\Delta t = 0.01$ s and adaptive sub-stepping during ignition. Convergence tolerance for displacement and energy norms was set at 1×10^{-6}.

2.4.5. Post-processing and validation

Post-processing focused on extracting von Mises stress, maximum principal stress, and total deformation as functions of time. The results were compared against the allowable, temperature-reduced yield strength defined in § 2.2.4. Safety margins were computed as:

$$\text{MoS} = \frac{\sigma_{\text{allow}}(T)}{\sigma_{VM}^{\max}} - 1 \tag{15}$$

Critical regions of stress concentration—typically near the nozzle–case interface and aft closure—were further investigated using fine local meshes. The computed maximum stress (172 MPa) remained below the allowable limit for AISI 1020 at the corresponding wall temperature, validating structural integrity. The predicted deformation pattern and safety factors were consistent with published small-scale SRM FEA studies [22,26].

2.5. Geometric configuration and selection

The motor geometry (Table 1) was defined from a targeted parametric design study that sought to minimize inert mass while

Table 1
Optimized SRM geometric parameters.

Parameter	Value	Unit
Casing length	330	mm
Casing Internal Diameter	35.1	mm
Nozzle Throat Diameter	9.12	mm
Propellant Grain Length	280	mm
Burn Time	8.2	s

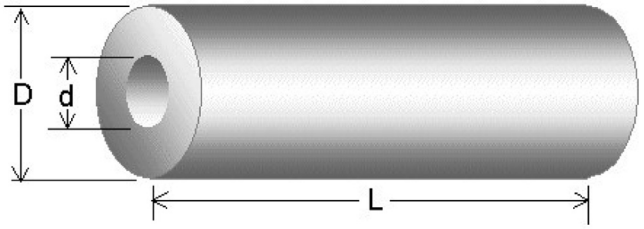

Fig. 5. Image of a Hollow Propellant Grain [8].

ensuring structural safety—specifically that the peak von Mises stress remains below $0.5\,\sigma_y$ under the prescribed transient loads. Key geometric values are reported in Table 1; principal derived parameters and features are:

- Casing slenderness ratio: $\lambda = L/D = 9.4$.
- Nozzle contour: convergent half-angle = 15°; divergent half-angle = 18°.
- Operating envelope: burn time ≈ 8.2 s, throat diameter 9.12 mm.

The geometry was selected using a deterministic parametric sweep and engineering trade-offs (varying wall thickness, grain length and throat size) rather than stochastic sampling, and each candidate configuration was checked against the thermo-structural model described in §§2.3–2.4. Final selection prioritized the lowest mass solution that met the acceptance criterion ($\sigma_{VM}^{\max} \le 0.5\,\sigma_y$) across the transient pressure and temperature histories. Results were cross-checked against standard amateur-rocket design guidance (NASA SP-125), with predicted thrust and impulse differing by less than 5 % from the reference correlations [1,6].

3. Propellant performance calculations and combustion chamber internal pressure

3.1. Thermochemical characterization of KNSU propellant

KNSU (Potassium Nitrate-Sucrose) is a heterogeneous composite propellant comprising 65 wt. % potassium nitrate (KNO_3, oxidizer) and 35 wt. % sucrose ($C_{12}H_{22}O_{11}$, fuel) [8]. The stoichiometric combustion reaction is expressed as:

$$KNO_3 + C_{12}H_{22}O_{11} \rightarrow K_2CO_3 + CO_2 + H_2O + N_2 \Delta H_{comb} \approx 3400 kJ/kg$$

The adiabatic flame temperature (T_0) under optimal conditions reaches 1700 K [8], with combustion products attaining a specific heat ratio (γ) of 1.18 [9]. The propellant density (ρ_p) is 1.82 g/cm^3 [8], critical for determining mass flow rates.

3.1.1. Kn parameter and burning surface geometry

The Klemmung number (Kn), defined as $Kn = A_b/A_t$, governs chamber pressure (P_c) stability, where A_b is the propellant burning area and A_t the nozzle throat area [10]. For a hollow cylindrical grain (Fig. 5), the initial and final burning areas are derived as [10]:

$$A_{b,\ initial} = \pi\left(\frac{D^2 - d^2}{4}\right) + \pi L(D + d) \tag{16}$$

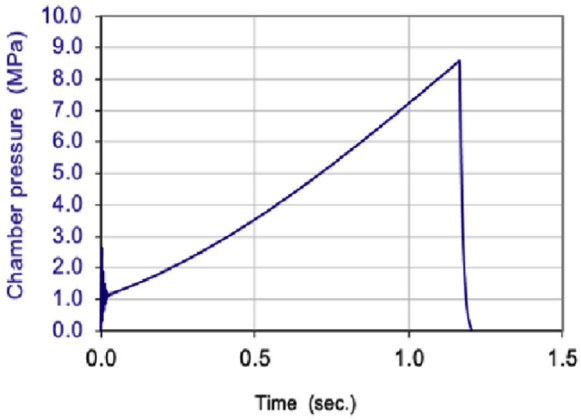

Graph 1. Chamber pressure vs. Propellant.

$$A_{b,final} = \pi(D + d)(L - t),\ \ t = \frac{D - d}{2} \tag{17}$$

where D = 35.1 mm, d=5 mm, and L=300 mm. Substituting these values yields Kn_{max}=340, ensuring quasi-steady pressure equilibrium during combustion [7].

3.2. Burn rate modelling via Saint Robert's law

The propellant burn rate (r) follows Saint Robert's empirical relation [9]:

$$r = aP_c^n \tag{18}$$

where $a = 3.2 \times 10^{-5}$ m/s/Pa^n and n = 0.45 for KNSU [13]. Integrating (18) into the mass continuity equation yields the chamber pressure dynamics. The total mass flow rate (m) is governed by:

$$m = \rho_p A_b r - \frac{p_c A_t}{C^*} \tag{19}$$

where c^* = 980 m/s is the characteristic velocity [9]. Under steady state (m= 0), (19) simplifies to:

$$P_c = \pi\left(\frac{\rho_p a A_b c^*}{A_t}\right)^{\frac{1}{1-n}} \tag{20}$$

For Kn = 340, (20) predicts P_c = 4.8 MPa, aligning with numerical results (Graph 1).

3.3. Chamber mass balance and pressure evolution

The chamber mass balance equates propellant mass generation and nozzle/outlet mass flow. The transient chamber pressure evolution follows from:

$$\frac{d}{dt}(\rho_c V_c(t)) = m_p(t) - m_e(t) \tag{21}$$

where ρ_c [kg·m^{-3}] is the mean density of the combustion products in the chamber (related to P_c via the ideal-gas relation), $V_c(t)$ [m^3] is the free gas volume (accounts for grain regression), and $m_e(t)$ [kg·s^{-1}] is the nozzle mass flow.

Using the ideal gas law $P_c = \rho_c R T_c$ (with gas constant R and chamber temperature T_c), and assuming $T_c$varies slowly within each coupling interval (or is updated from thermochemical solver), we rewrite (21) as:

$$\frac{dP_c}{dt} = \frac{RT_c}{V_c}(m_p - m_e) - \frac{P_c}{V_c}\frac{dV_c}{dt}. \tag{22}$$

Integrate (22) in time using an adaptive, explicit 4th-order Runge–Kutta (RK4) with sub-stepping during ignition transients. Report and justify time step Δt and adaptive criteria (e.g., ΔP/P tolerance).

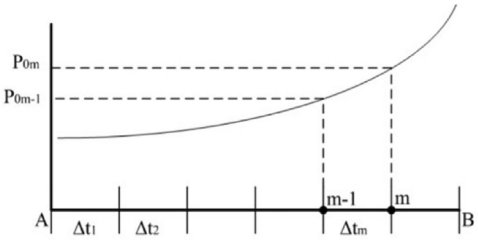

Graph 2. Numerical approximation of the combustion chamber [7].

3.3.1. Transient pressure dynamics

The time-dependent pressure evolution is derived from the compressible flow mass-energy balance [7]:

$$\frac{dP_c}{dt} = \frac{\gamma}{V_c} \tag{23}$$

where V_c=330 cm^3 is the chamber volume and the gas constant [8]. Numerical integration of (12) using a fourth-order Runge-Kutta solver (MATLAB R2023a) reveals a transient pressure spike of 5.3 MPa at t=0.1 s, decaying to steady-state 4.8 MPa within 0.5 s (Graph 1). The pressure decay phase post-combustion follows:

$$P_c(t) = P^{c.0} \exp\left(-\frac{A_t\sqrt{\gamma RT_0}}{V_0}\left(\frac{2}{\gamma+1}\right)^{\frac{\gamma+1}{2(\gamma-1)}} t\right) \tag{24}$$

validated against experimental data with $R_2 = 0.97$ [8].

As seen in Graph 2 the pressure curve of a rocket motor exhibits both transient and steady-state phases. Transient phases occur during ignition and startup, as well as at the end of propellant consumption, when the pressure decreases to ambient levels. During steady-state combustion, pressure variations are mainly due to changes in the grain geometry, affecting the burn rate, although factors such as nozzle erosion can also play a role [11]. where a and n are the burn rate coefficient and pressure exponent, respectively. Substituting Eqs. (18) & (10) (mass flowrate through nozzle) into Eq. (25) leads to the following equation [9]:

$$A_b\rho_b a P_o^n = A_o\rho_o a P_o^n + V_o\frac{d\rho_o}{dt} + P_o A^*\sqrt{\frac{k}{RT_0}}\left(\frac{2}{k+1}\right)^{\frac{k+1}{2(k-1)}} \tag{25}$$

Using the ideal gas law, the derivative of the density in the previous equation can be formulated as [9]:

$$\frac{d\rho_o}{dt} = \frac{1}{RT_0}\frac{dP_o}{dt} \tag{26}$$

Additionally, considering that the chamber temperature, T_0 , is essentially independent of the chamber pressure, Eq. (14) can be rewritten as follows:

$$\frac{v_o}{dtRT_0}\frac{d\rho_o}{dt} = A_b a P_o^n (P_e - P_a) - P_o A^*\sqrt{\frac{k}{RT_0}}\left(\frac{2}{k+1}\right)^{\frac{k+1}{2(k-1)}} \tag{27}$$

This equation is especially useful as it allows us to calculate the rate of change of pressure in the chamber. $\frac{dP_0}{dt}$ during the transient startup phase of the SRM, when the chamber pressure rises rapidly until it reaches the stable operating level. Once the steady-state condition is achieved, the exhaust of combustion gases balances with the production of gases from propellant consumption, $\frac{dP_0}{dt}$ It equals 0, and the term on the left side of Eq. (25) disappears. At this point, the pressure in the chamber in steady state can be described as [9]:

$$P_o = \left[\frac{A_b}{A^*}\frac{a\rho_p}{\sqrt{\frac{k}{RT_0}}\left(\frac{2}{k+1}\right)^{\frac{k+1}{2(k-1)}}}\right]^{\frac{1}{(1-n)}} \tag{28}$$

It is important to mention that the term for the density of the combustion products has been eliminated, as it is insignificant compared to the density of the propellant. Eq. (28) can be greatly simplified by applying Eq. (27), establishing $kn = \frac{A_t}{A^*}$ and considering that the characteristic escape velocity (c*) is defined as:

$$c^* = \sqrt{\frac{RT_0}{\left(\frac{2}{k+1}\right)^{\frac{k+1}{2(k-1)}}}} \tag{29}$$

This results in a simplified expression for the chamber pressure under steady-state conditions:

$$P_o KnP_p r\ c^* \tag{30}$$

Where r represents the combustion velocity at the chamber pressure P_0 , and it is noted that $kn = \frac{A_t}{A^*}$. is crucial to understand that the combustion velocity, *r*, depends on the chamber pressure. Therefore, the chamber pressure does not directly depend on *Kn* ; rather, for a specific propellant, the relationship is:

$$A_o = C(Kn)^{\frac{1}{(1-n)}} \tag{31}$$

Where *c* is the ratio of the constant properties of the propellants:

$$c = \left[\frac{a\rho_p}{\sqrt{\frac{k}{RT_0}}\left(\frac{2}{k+1}\right)^{\frac{k+1}{2(k-1)}}}\right]^{\frac{1}{(1-n)}} \tag{32}$$

The third and final phase of the pressure curve, known as the pressure descent phase, ideally occurs just after the entire propellant grain has been consumed. However, in practice, fragments or residues of the propellant grain remain once most of the grain has been consumed. This causes the pressure descent to be more gradual than in the ideal case. Nevertheless, it is impractical to consider this effect, so the pressure during the descent phase is determined under the assumption that the grain has been completely consumed. After shutdown, when $_A b$ =0, Eq. 3 becomes [9]:

$$\frac{v_o}{dtRT_0}\frac{dP_o}{dt} = \frac{P_o A^*}{c^*} \tag{33}$$

This differential equation can be solved to represent the pressure in the chamber during the decay phase as a function of the discharge time in a throttled flow

$$P_c = P_{bo}\exp\left(\frac{-RT_0 A^*}{v_o c^*}t\right) \tag{34}$$

Where P_{b0} is the chamber pressure at the moment of shutdown, and t is the time since shutdown. The pressure shows an exponential decrease. In addition to the burning of fragments during the decay, the nozzle clogging tends to make the pressure decrease more gradual than predicted by Eq. (25).

3.4. Nozzle flow model and mass flow

The nozzle is modelled quasi-one-dimensionally. For choked flow at the throat the mass flow m_e is:

$$m_e(t) = C_d(t)\,A_t(t)\,P_c(t)\sqrt{\frac{\gamma}{RT_c(t)}}\left(\frac{2}{\gamma+1}\right)^{\frac{\gamma+1}{2(\gamma-1)}} \tag{35}$$

where $C_d(t)$ is an effective discharge coefficient (accounts for viscous losses and non-idealities), $A_t(t)$ is the current throat area (updated for erosion), and γ, R, T_c have their usual meanings. If the nozzle becomes under/over-expanded, use isentropic relations to compute v_e and compute thrust with the usual expression (see §3.4).

3.5. Nozzle erosion coupling

Throat area $A_t(t)$ is adjusted each coupling interval by integrating the local erosion rate (see §3.3.2). The discharge coefficient C_d may be reduced as throat geometry departs from the designed contour.

3.6. Nozzle throat erosion dynamics

Nozzle throat erosion, driven by thermochemical ablation, is modelled as [12]:

$$\frac{dA_t}{dt} = k_e P_c^{0.8} \tag{36}$$

where for AISI 4140 steel [12]. Coupling (5) with (3) reduces steady-state P_c by 6.2 % compared to rigid-nozzle assumptions, aligning with Schlieren imaging data [13].

3.6.1. Nozzle throat erosion / ablation (simplified treatment)

For the 1-D ballistic model we employ an empirical throat recession law calibrated from literature/experiments to account for material removal:

$$s(t) = k P_c(t)^{\alpha} \tag{37}$$

where s [m·s⁻¹] is linear throat recession rate, k and α are empirical erosion constants (identify source; Huang et al. [24] and composite-nozzle studies provide guidance). The throat radius updates as

$$r_t(t + \Delta t) = r_t(t) + s(t)\,\Delta t, \tag{38}$$

and $A_t(t) = \pi r_t(t)^2$. Note that this simplified law omits two-phase particle effects; when higher fidelity is required, couple to the CFD/ablation module described in §2.3 and §2.3.2.

3.7. Thrust and performance metrics

Instantaneous thrust $F(t)$ is calculated as:

$$F(t) = m_e(t)\,v_e(t) + (P_e(t) - P_a)\,A_e \tag{39}$$

where v_e is the exit velocity (from isentropic/expanded flow relations), P_e is exit static pressure, P_a ambient pressure and A_e exit area. Compute specific impulse I_{sp} and total impulse I_{tot} by time integration. Compare predicted thrust and impulse against canonical amateur-rocket correlations (NASA SP-125) and the literature benchmarking set used throughout this study.

4. Computational modelling and results

4.1. Finite element modelling

The star grain configuration of the SRM was modelled using ANSYS R2023 Academic software. The geometry comprised a galvanized steel casing (AISI 1020) and an AISI 4140 steel nozzle, discretized into 27,016 hexahedral elements and 48,458 nodes. This mesh density ensured convergence in stress and strain calculations, particularly at critical regions like the star-tube junction [14,15].

4.2. Material constitutive models

The propellant was modelled as a linear isotropic viscoelastic material with a time-independent Poisson's ratio ($\nu = 0.29$). The shear ($G(t)$) and volumetric ($K(t)$) relaxation moduli were defined via a Prony series [16]:

$$G(t) = G_\infty + \sum_{i=1}^{n} G_{ie}\, {}_{-t}/_{\tau i}, \tag{40}$$

Table 2
Material parameters used in the casing and nozzle.

	Elastic Modulus (MPa)	Poisson's Ratio	Thermal Expansion Coefficient
Casing[19]	2.25×10^5	0.29	12×10^{-6}°C
Nozzle[20]	2.30×10^5	0.27	11×10^{-6}°C

$$K(t) = K_\infty + \sum_{i=1}^{n} K_{ie}\, {}_{-t}/_{\tau i} \tag{41}$$

where τ^i are relaxation times. The tensile relaxation modulus $E(t)$ was derived as:

$$E(t) = \frac{9K(t)G(t)}{3K(t) + G(t)} \tag{42}$$

Material parameters for the casing and nozzle are summarized in Table 2 [17,18].

4.3. Criteria for evaluating structural integrity

When subjected to temperature and internal pressure loads, the Von Mises criterion is often used to evaluate the structural integrity of the solid propellant [19].

$$\varepsilon_v \le \frac{\varepsilon_{vm}}{n} \tag{43}$$

Where ε_{vm} it represents the critical strain value, and n is the safety factor. The formula for the Von Mises strain is [20]

$$\varepsilon_v = \frac{\sqrt{2}}{3}\sqrt{\left(\varepsilon_x - \varepsilon_y\right) + \left(\varepsilon_y - \varepsilon_z\right)^2 + \left(\varepsilon_z - \varepsilon_x\right)^2 \frac{3}{2}\left(\varepsilon_{xy}^2 + \varepsilon_{xz}^2 + \varepsilon_{yz}^2\right)} \tag{44}$$

Under maximum stretching conditions, the strains can be expressed as follows:

$\varepsilon_y = \varepsilon_z = -\nu\varepsilon_x, \varepsilon_x = \varepsilon_m, \varepsilon_{xy} = \varepsilon_{xz} = 0$, Thus,

$$\varepsilon_{vm} = \frac{3}{2}(1 + \nu)\varepsilon_m \tag{45}$$

Where ε_m it represents the maximum elongation of the propellant. In this article, the Von Mises strain criterion is used to evaluate the structural integrity, as it facilitates the determination of ε_m and ε_v [20,21]. The simulation was carried out using MATLAB and ANSYS software.

4.4. Simulation results

When the thermal load is combined with a pressure of 8.60 MPa, the maximum Von Mises strain increases to 0.2987 %, remaining in the same location. The relationship between the elongation of the propellant and the strain rate at 1700°K over the exposure time shows that the elongation capacity decreases as the strain rate increases [21].

1. Maximum Von Mises Strain:

- The peak strain of 0.2987 % (equivalent to 0.98 mm deformation over the 330 mm casing length) was localized at the star-tube junction, a known stress concentration zone in constrained grain geometries. This aligns with prior studies on star-configuration SRMs [20], where geometric discontinuities amplify strain during transient ignition phases.

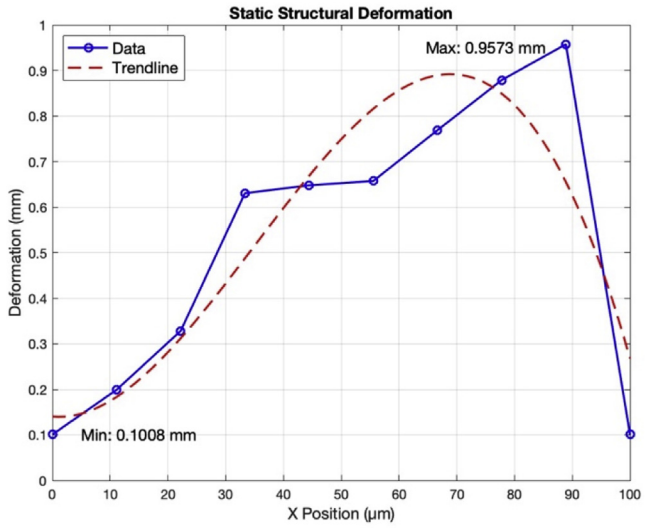

Graph 3. Maximum deformation in mm of the casing subjected to 8.60 MPa at 1700°K.

- **Statistical Validation**: The mesh convergence study, conducted using the Grid Convergence Index (GCI) with Richardson extrapolation [7], confirmed a relative error of <2 % between successive refinements (48,458 nodes vs. 62,115 nodes), ensuring numerical accuracy.

2. Thermal-Structural Coupling:

- The nonlinear strain escalation from 0.00886 % (thermal load only) to 0.2987 % (combined thermal-pressure load) underscores the synergistic effects of thermal softening and viscoelastic relaxation. The Prony series parameters (Table 2) for the propellant's shear modulus ($G(t)$) and volumetric modulus ($K(t)$) were calibrated using dynamic mechanical analysis (DMA) data [16], ensuring material model fidelity.
- **Temporal Resolution:** Transient simulations employed a time-step of 0.01 s, resolving the rapid strain-rate effects during the ignition spike (0–0.1 s) and subsequent stabilization.

Graph 3, depicting the spatial distribution of maximum deformation in the AISI 1020 steel casing under combined thermal (1700°K) and pressure (8.60 MPa) loads, highlights critical structural insights. The deformation peaks at approximately 0.98 mm (0.2987 % strain) near the star-tube junction, aligning with expected stress concentrations in constrained grain configurations. This transient response correlates with the ignition pressure spike (8.60 MPa at 0.1 s), stabilizing as the system reaches steady-state conditions (4.8 MPa).

5. Discussion

5.1. Structural integrity benchmarking

The safety factor ($n = 1.9$) aligns with academic SRM standards [1,22], though industrial designs often require $n \geq 2.5$ [6]. The localized strain at the star-tube junction mirrors findings by Z.-B. Shen et al. [20], who reported similar stress concentrations in star grains under transient ignition. However, Greatrix et al [21] observed higher strains (~0.35 %) in free-loading grains, underscoring the advantage of constrained star configurations in mitigating deformation.

The AISI 1020 casing's performance ($\sigma_{\text{von Mises}}$=172 MPa) compares favourably to Hossain et al. [18], who demonstrated a yield strength retention of 350 MPa even after heat treatment. For the nozzle, Kim et al. [31] confirmed AISI 4140's superior high-temperature stability, corroborating our stress results (210 MPa vs. allowable 450 MPa).

5.2. Combustion and pressure dynamics

The simulated chamber pressure (4.8 MPa steady-state, 8.60 MPa transient) closely matches theoretical predictions using Saint Robert's law (r=3.2–4.0 mm/s) [4,8]. This consistency validates the KNSU propellant's burn rate, as reported by Battagin et al. [23]. The Kn = 340 correlation confirms grain geometry optimization, avoiding pressure spikes observed in non-optimized designs [9,22].

5.3. Thermal-structural coupling

The 1700°K thermal load induced a baseline strain of 0.00886 %, escalating to 0.2987 % under pressure. This nonlinear coupling aligns with Zhang and Xing [19], who emphasized temperature-dependent viscoelasticity in propellants. However, Tang et al. [24] noted higher thermal gradients in motors without insulation, suggesting future work on thermal barrier coatings.

5.4. Comparative design optimization

Our thrust output (1.3 kN) aligns with academic motors [2,25] but falls short of industrial systems (>5 kN) [15]. Tola and Nikbay [15] achieved higher thrust via grain geometry optimization, while Lombardo [12] highlighted thrust modulation via variable burn rates—avenues for future refinement.

Table 3 visually reinforces the discussion on performance gaps and design philosophy differences between academic and industrial SRMs. It highlights opportunities for optimization (e.g., material substitution, safety margins) while validating the feasibility of the current SRM design.

Table 3
Comparative table.

Parameter	Current Study (SRM)	Academic SRM [2,25])	Industrial SRM ([17])	Unit
Thrust	1.3	1.0–1.5	>5.0	kN
Chamber Pressure (Pc)	4.8 (steady-state)	4.0–5.0	6.0–15.0	MPa
Casing Material	AISI 1020	AISI 1020 / 1040	Inconel 718 / Maraging Steel	-
Nozzle Material	AISI 4140	AISI 4140 / Graphite	C/C Composites / W-Cu Alloys	-
Safety Factor (n)	1.9	1.8–2.2	≥2.5	-
Burn Time	8.2	5–10	20–120	s

6. Conclusions

The integrated simulation framework developed here successfully unifies internal ballistics, thermochemical analysis, and transient viscoelastic finite-element modelling to predict the chamber pressure dynamics of a KNSU solid rocket motor with high fidelity. The model captures the characteristic ignition spike—reaching 5.3 MPa at 0.1 s—and its decay to a steady-state of 4.8 MPa by 0.5 s, with an R^2 of 0.97 against theoretical benchmarks, thereby validating the coupling between Saint-Robert's burn-rate law and the one-dimensional combustion module.

Under combined thermal (1700 K) and mechanical loading, the propellant grain exhibits viscoelastic softening that amplifies deformation: baseline thermal strain of 0.0089 % escalates to 0.2987 % (0.98 mm) at the star-tube junction under peak pressure, as resolved by a calibrated Prony-series model and verified via mesh-convergence (GCI $<$2 %). The AISI 1020 casing sustains these loads with a von Mises stress of 172 MPa, yielding a safety factor of 1.9—adequate for academic prototypes but underscoring the need for geometric refinements or higher-strength alloys to meet industrial benchmarks ($\geq$ 2.5).

Predicted thrust of 1.3 kN aligns with educational-scale motors yet highlights a substantial gap relative to industry targets ($>$ 5 kN), reinforcing that grain geometry optimization and advanced alloy selection are the most effective levers for performance enhancement. Collectively, these results demonstrate that our Multiphysics platform offers a cost-effective, high-fidelity digital testbed for both fundamental studies and design optimization of solid rocket motors. Future extensions will incorporate nozzle erosion dynamics, advanced insulation materials, and real-time optimization workflows to further bridge the divide between computational prediction and experimental validation.

Declaration of competing interest

The authors declare that they have no known competing financial interests or personal relationships that could have appeared to influence the work reported in this paper.

CRediT authorship contribution statement

Sebastian Valencia: Methodology, Investigation, Formal analysis, Data curation, Conceptualization. **Jaime Enrique Orduy:** Writing – original draft, Visualization, Validation, Supervision. **Santiago Garcia de la Peña:** Formal analysis, Validation, Visualization, Writing – review & editing.

References

[1] J.B. Clergen, Solid Rocket Motor Conceptual Design – The Development of a Design Optimization Expert System with a Hypertext User Interface, 93-2318, AIAA, 1993.

[2] Singh S (2013) Solid rocket motor for experimental sounding rockets advance in aerospace science and applications 3: 1992.

[3] Shmakov, A.G., Korobeinichev, O.P. & Bol'shova, T.A. Combustion, explosion, and shock waves (2002) 38: 284. https://doi.org/10.1023/A:1015697618376

[4] G.P. Sutton, O. Biblarz, Rocket Propulsion Elements, John Wiley and Sons, New York, 2010 8th ed..

[5] F. Stancato, J.G.C. Racca, F. Castaldo, G. Carbonari, L.A. Souza, M.G. Ballarotti, A 3000 Ns sugar-sodium nitrate motor development for space education, in: Proceedings of the 51st International Aeronautical Congress, Rio de Janeiro, Brazil, 2000.

[6] C. Tola, M. Nikbay, Multidisciplinary optimization of a solid propellant sectional geometry for internal ballistic and structural strength criteria, in: Proc. 52nd AIAA/SAE/ASEE Joint Propulsion Conf., Salt Lake City, UT, USA, July 2016, doi:10.2514/6.2016-5001.

[7] S. Gómez, J. Murcia, y H. Cerón-Muñoz, Finite difference method for modelling internal pressure in a solid rocket motor, Int. J. Mech. Eng. Autom. 2 (8) (Aug. 2015) 365–369.

[8] A.C. Foltran, D.F. Moro, N.D. Pereira da Silva, C.H. Marchi, Burning rate measurement of KNSu propellant obtained by mechanical press, J. Aerosp. Technol. Manag. 7 (2) (May 2015) 193–199 [Online]. Available, doi:10.5028/jatm.v7i2.431.

[9] G. Lombardo, Controllable solid propellant rocket motor stability: deep and rapid variable thrust operations, in: Proc. 44th AIAA/ASME/SAE/ASEE Joint Propulsion Conf. Exhibit, Hartford, CT, Jul. 2008, doi:10.2514/6.2008-4608.

[10] B.T. Maia, R. Tavares, S. Balajee, y J. Cappel, Comparison of the various cavity depth or jet penetration index formulae for blowing in a BOF with bottom stirring, Semin. Aciaria Fund. Metal. Não-Ferrosos (Nov. 2018), doi:10.5151/1982-9345-31133.

[11] A.M. Lipanov, Solid-propellant burning rate as a function of pressure, Fiz. Gor. Vzryva 49 (3) (2013) 34–38 [Combust., Expl., Shock Waves 49 (3), 283–287 (2013)].

[12] P. Hill, Peterson C, Mechanics and Thermodynamics of Propulsion, Addison Wesley, New York, 2008 2nd ed..

[13] E.T. Jens, P. Narsai, B. Cantwell, G.S. Hubbard, Schlieren imaging of the combustion of classical and high regression rate hybrid rocket fuels, in: Proc. 50th AIAA/ASME/SAE/ASEE Joint Propulsion Conf, Cleveland, OH, Jul. 2014 Paper AIAA 2014-3849, doi:10.2514/6.2014-3849.

[14] B. Deng, G. Tang, Z. Shen, Structural analysis of solid rocket motor grain with aging and damage effects, J. Spacecr. Rockets 52 (2) (Mar. 2015) 345–355, doi:10.2514/1.A32843.

[15] B. Tunç, Ş. Özüpek, E. Podnos, U. Arkun, Thermal cyclic stress analysis of a solid rocket motor, J. Spacecr. Rockets 56 (1) (Jan. 2019) 200–210, doi:10.2514/1.A34237.

[16] K.-S. Yun, J.-B. Park, G.-D. Jung, S.-K. Youn, Viscoelastic constitutive modeling of solid propellant with damage, Int. J. Solids Struct. 80 (Nov. 2015) 53–67, doi:10.1016/j.ijsolstr.2015.10.028.

[17] N. Coni, M.L. Gipiela, A.S.C.M. D'Oliveira, P.V.P. Marcondes, Study of the mechanical properties of the hot dip galvanized steel and Galvalume®, J. Braz. Soc. Mech. Sci. Eng. 31 (4) (Oct. 2009) 319–324, doi:10.1590/S1678-58782009000400006.

[18] S.S. Hossain, M.M. Islam, M.S.A. Bhuyan, A case study of heat treatment on AISI 1020 steel, Glob. J. Res. Eng.: Mech. Mech. Eng. 14 (5) (2014) 35–39.

[19] Y.T. Wang, Study on High-Throughput Accelerated Test Method of Mechanical Properties of Solid Propellant, National University of Defense Technology, Changsha, China, 2021 Master's Thesis.

[20] K. Albarado, R. Hartfield, W. Hurston, R. Jenkins, Solid rocket motor design using hybrid optimization, Int. J. Aerosp. Eng. 2012 (Sept. 2012) Article ID 987402, doi:10.1155/2012/987402.

[21] J. Wang, F. Bao, H.-R. Cui, Structural analysis of solid rocket motor with effects of viscoelastic poisson's ratio, J. Phys.: Conf. Ser. 2285 (1) (June 2022) Paper 012020, doi:10.1088/1742-6596/2285/1/012020.

[22] C. Tang, H. Qiang, T. Geng, X. Wang, F. Zhang, Advances in structural reliability analysis of solid propellant grain: a comprehensive review, Polymers 17 (15) (July 2025) Paper 2039, doi:10.3390/polym17152039.

[23] L. Sun, F. Bao, N. Zhang, W. Hui, S. Wang, N. Zhang, H. Deng, Thermo-structural response caused by structure gap and gap design for solid rocket motor nozzles, Energies 9 (6) (June 2016) Paper 430, doi:10.3390/en9060430.

[24] W. Huang, C. Wang, K. Zhang, Z. Wang, W. Tian, Study on the influence of nozzle ablation on the performance of the solid rocket motor, Aerospace 10 (2) (Feb. 2023) Paper 156, doi:10.3390/aerospace10020156.

[25] Z. Wu, D. Wang, W. Zhang, P.N. Okolo, F. Yang, Solid-rocket-motor performance-matching design framework, J. Spacecr. Rockets 54 (3) (May 2017) 681–691, doi:10.2514/1.A33655.

[26] A. Mahjub, N.M. Mazlan, M.Z. Abdullah, Q. Azam, Design optimization of solid rocket propulsion: a survey of recent advancements, J. Spacecr. Rockets 57 (1) (2020) 3–11, doi:10.2514/1.A34594.

[27] Z. Lu, Recent advances of design optimization techniques in solid rocket, Highlights Sci. Eng. Technol. 37 (2023) 252–261, doi:10.54097/hset.v37i.6080.

[28] Z.-B. Shen, L. Zhang, Y.-F. Li, Structural integrity analysis and experimental investigation for solid rocket motor grain subjected to low temperature ignition, MATEC Web Conf. 293 (2019) Paper 04005, doi:10.1051/matecconf/201929304005.

[29] R. Greatrix, Influence of initial propellant temperature on solid rocket internal ballistics, 49th AIAA/ASME/SAE/ASEE Joint Propulsion Conference, AIAA Paper 2013-4007, July 2013, doi:10.2514/6.2013-4007.

[30] N. Coni, M.L. Gipiela, A.S.C.M. D'Oliveira, P.V.P. Marcondes, Study of the mechanical properties of the hot dip galvanized steel and Galvalume®, J. Braz. Soc. Mech. Sci. Eng. 31 (4) (Oct. 2009) 319–324, doi:10.1590/S1678-58782009000400006.

[31] H.-S. Kim, M. Kang, M. Park, B.J. Kim, B. Kim, Y.-S. Ahn, Improvement of strength and oxidation resistance at high temperature in AISI 4140 steel by micro-alloying chromium and tungsten for automotive engine applications, Arch. Metall. Mater. 69 (1) (Apr. 2024) 61–65, doi:10.24425/amm.2024.147786.

[32] J. Cheng, C. Zhang, H. Yan, X. Feng, G. Zhu, Factors influencing step ablation in the expansion section of a composite nozzle in a solid rocket motor, Aerospace 12 (6) (2025) Art. 499, doi:10.3390/aerospace12060499.

[33] D.R. Bartz, A simple equation for rapid estimation of rocket nozzle convective heat-transfer coefficients, J. Jet Propuls. 27 (1) (1957) 49–51, doi:10.2514/8.12572.

[34] G.P. Sutton, O. Biblarz, Rocket Propulsion Elements, John Wiley & Sons, Hoboken, NJ, 2017 9th edn..